Materials Characterization 171 (2021) 110822

Contents lists available at ScienceDirect

Materials Characterization

journal homepage: www.elsevier.com/locate/matchar

The effect of grain size on bubble formation and evolution in helium-irradiated Cu-Fe-Ag

Michael Wurmshuber [a,*], David Frazer [b,c], Mehdi Balooch [b], Inas Issa [a], Andrea Bachmaier [d], Peter Hosemann [b], Daniel Kiener [a]

[a] Department Materials Science, Montanuniversität Leoben, Jahnstraße 12, 8700 Leoben, Austria
[b] Department of Nuclear Engineering, University of California, Berkeley, 4155 Etcheverry Hall, Berkeley, CA 94720, USA
[c] Advanced Characterization and PIE, Idaho National Laboratory, 1955 N. Fermont Ave, Idaho Falls, ID 83415, USA
[d] Erich-Schmid Institute of Materials Science, Austrian Academy of Sciences, Jahnstraße 12, 8700 Leoben, Austria

ARTICLE INFO

Keywords:
Nanostructured materials
Helium implantation
Helium bubbles
Swelling
Nanoindentation

ABSTRACT

Nanostructured metals are a promising candidate for future applications in irradiative environments, such as nuclear energy facilities, due to a conceivable tolerance against radiation damage. As the presence of helium irradiation is frequently unavoidable, e.g. in nuclear fusion facilities, the effect of helium on the properties of nanostructured materials is of immanent interest. In this work, ultra-fine grained (UFG; 100 nm grain size) and nanocrystalline (NC; 20 nm grain size) Cu-Fe-Ag samples have been implanted with various fluences of helium and were investigated regarding helium-induced modifications using atomic force microscopy, nanoindentation and transmission electron microscopy. While for these nanostructured materials a tolerance against radiation damage has been reported earlier, we find that the influence of helium on swelling and mechanical properties is not negligible. The increased amount of closely spaced interfaces in the NC material provides swift diffusion paths of helium, thereby facilitating bubble nucleation in the early stages of irradiation. For high fluences of helium, however, the smaller grain size and larger amount of nucleation sites in the NC composite restrict the growth of individual bubbles, which has a positive effect on swelling and counteracts mechanical property degradation compared to UFG and conventional coarse-grained materials. As such, our investigations on immiscible Cu-Fe-Ag nanocomposites pave a promising strategy for designing novel highly radiation enduring materials for irradiative environments.

1. Introduction

Driven by the desire to mitigate climate change and steer the world into a greener future, numerous advances and new concepts in the sector of power engineering are being developed. As nuclear energy yields a high energy output and little emissions, ongoing developments in this field are promising to contribute to the solution of the energy discussion [1,2]. Gen IV fission reactors and fusion reactors provide a truly challenging environment for the materials considered in these systems [3–6]. The problem of accumulating radiation damage in materials has been widely addressed, and it was found that nanostructured metals are experiencing a favorable response to high radiation doses [7–15]. This radiation tolerant behavior originates in the large amount of closely spaced interfaces within the material, which can act as sinks to the radiation-induced lattice defects. In addition to displacement damage, the generation of helium due to nuclear reaction or direct exposure to a plasma can lead to materials degradation. CANDU reactors, for example, produce a large amount of He, leading to materials degradation in Ni-containing materials, such as X750 [16]. The insolubility of He in the matrix leads to phase separation and bubble formation within the material. Vacancies tend to migrate towards these bubbles, leading to underpressurization and growth of the bubbles and the consecutive formation of so-called He-vacancy clusters [17–19]. The bubbles or clusters inside the material naturally lead to reduction in the materials density and in turn to swelling and degradation of mechanical properties (e.g. embrittlement). Since the formation of excessive cavities in the material results in rapid materials property degradation, new nanostructured materials are developed and investigated [7,20–31]. Especially works on nanostructured Cu-based alloys have shown promising results [7,32–36]. Helium bubbles implanted in nanolayered Cu-Nb, Cu-

* Corresponding author.
E-mail address: michael.wurmshuber@unileoben.ac.at (M. Wurmshuber).

https://doi.org/10.1016/j.matchar.2020.110822
Received 26 August 2020; Received in revised form 24 November 2020; Accepted 10 December 2020
Available online 13 December 2020

V and Cu-Mo composites have been observed to be restricted in growth by the interfaces between the immiscible components, even after subsequent annealing. A combination of unbalanced vacancy distribution in the two materials and hindered interdiffusion between the two immiscible components has been proposed as the reason for bubble growth stopping at the interface [33]. In our previous work [15], an ultra-fine grained (UFG) and a nanocrystalline (NC) Cu-Fe-Ag alloy were developed, exhibiting enhanced tolerance against radiation damage. This work presented here goes a step further and utilizes the rapid throughput helium irradiation and testing technique developed here [21] to provide further insight into these materials under extreme conditions. The influence of both, grain size and helium content, on swelling and mechanical properties is investigated and a theory explaining the underlying bubble formation and growth mechanisms is proposed.

2. Experimental

2.1. Material selection, fabrication and characterization

The material system Cu-Fe-Ag investigated here is mainly used in electronic applications, e.g. as high-strength conductors [37–40] or giant magnetoresistors [41–43]. Notably, the three components Cu, Fe and Ag are immiscible and by applying severe plastic deformation the characteristic lengths of the material can be reduced to the submicron or nanoscale, respectively. Thus, the formation of a large amount of distinct phase boundaries is guaranteed. These interfaces are believed to play a significant role in the formation and growth of helium bubbles [7,33], rendering these nanocomposites ideal model materials to investigate the effects of interface density on helium-induced property deterioration. Moreover, this material has already been investigated in ultra-fine grained (UFG), nanocrystalline (NC) and nanoporous condition in terms of proton-radiation effects in earlier work [15]. There, a radiation tolerant behavior against displacement damage, originating in the vast amount of interfaces, was already successfully demonstrated.

The Cu-Fe-Ag was produced via a powder metallurgical route. The powders (50 at.% Cu, 25 at.% Fe and 25 at.% Ag) were compacted using vacuum hot-isostatic pressing (HIP). The material was then cut in disks and deformed in a high pressure torsion (HPT) tool until saturation [44]. Subsequently, the now supersaturated solid solution underwent two different heat treatments (400 °C for 1 h for the NC sample, 600 °C for 1 h for the UFG sample) to redistribute the phases and adjust grain size. A more detailed description of the precursor materials and sample fabrication processes is given in [15].

The resulting microstructure was investigated using a transmission electron microscope (TEM; CM12, Philips, Amsterdam, Netherlands), where energy-dispersive X-ray spectroscopy (EDX; 7426, Oxford Instruments plc, Abingdon, UK; Software EDAX) was used to characterize the chemical composition of the samples.

For a post-irradiation characterization of the microstructure, lift-outs were processed from helium-implanted areas using an Omniprobe 200 manipulator (Oxford Instruments plc, Abingdon, UK) in a dual-beam FIB-SEM (Auriga, Zeiss GmbH, Oberkochen, Germany). The lift-outs were investigated in a JEOL 2200FS TEM (JEOL Ltd., Akishima, Japan) in bright field and STEM mode.

2.2. Helium implantation

To investigate helium-induced swelling and related property changes, the UFG and NC samples were irradiated with 25 keV helium ions at room temperature using a helium-ion microscope (Orion NanoFab, Carl Zeiss GmbH, Oberkochen, Germany). Helium of various fluences ranging between 10^{17} and 10^{18} ions/cm^2 was implanted in several 10×10 μm^2 square fields on the polished material surface, with the dose rate calculated to be 1 dpa/min. The corresponding dose profiles in dpa, as well as resulting helium content (in atomic %), were simulated using the computer software "Stopping and Range of Ions in Matter" (SRIM) [45] and are displayed in Fig. 1. The K-P calculation mode was chosen with an displacement energy of 25 eV. Studies on pure Cu showed that after helium implantation with the exact same parameters, a helium bubble superlattice forms, therefore the sample temperature could not have exceeded 100 °C during the helium implantation [46,47].

2.3. Atomic force microscopy

An elegant and straightforward method to assess the swelling of materials subsequent to helium implantation is by using atomic force microscopy (AFM) to scan over the implanted region and compare the topologies in irradiated and unirradiated conditions. A Nanoscope III (Digital Instruments, Santa Barbara, USA) AFM was used to investigate the surface topology of the helium-implanted areas including their unirradiated surroundings in tapping mode.

2.4. Nanoindentation experiments

Characterizing the local changes in mechanical properties of materials exposed to helium implantation is a challenging task. The limited penetration depth of the He ions in the range of 200 nm (as apparent in Fig. 1) calls for small-scale testing methods to assess the helium-induced property changes without probing too much unirradiated material volume. Depth-sensing nanoindentation provides several advantages in this field, such as comparably straight-forward and fast sample preparation, and the possibility to measure hardness and elastic modulus continuously throughout the indentation process by using Continuous Stiffness Measurement (CSM) indentation [48–51]. The drawbacks of an extended plastic zone and, consequently, the sampling of convoluted properties of modified material on top and unaltered material beneath can be estimated and accounted for using plastic zone size models [52–57]. A TI 950 Triboindenter (Hysitron Inc., Eden Prairie, USA) with an in-situ scanning probe microscopy (SPM) option and equipped with a diamond Berkovich tip was used to perform the nanoindentation in this work. After the tip calibrations were performed following the procedure of Oliver & Pharr [48], the topology of the regions of interest on the specimens were mapped using the in-situ SPM option, allowing indents to be placed with a 10 nm accuracy. The CSM indentations were performed to peak loads of 6000 μN and 9000 μN for UFG and NC material, respectively. This was selected in order to achieve a final indentation depth of approximately 250 nm in both material conditions. As the implantation depth of the helium ions should be the same in both materials, we expect similar fractions of irradiated and unirradiated material in the bulk response, making the results and general hardening behavior immediately comparable. For each fluence of He irradiation, five indents were performed in the helium-implanted squares, as well as several control indents in the surrounding unimplanted material.

3. Results

3.1. Microstructure and chemical composition

TEM bright field images of the final microstructure of UFG and NC material, as well as their respective selective area electron-diffraction (SAD) patterns, are presented in Fig. 2. The grain size of the NC material batch was measured to be 18.8 ± 1.8 nm using the grain intercept method. The grain size for the other material (95.7 ± 10.3 nm) actually lies on the boundary between UFG and NC regime (~100 nm). Still, the term UFG was chosen for easier differentiation. The clearly separated rings in the SAD patterns indicate that the heat treatment used to tune the grain size after HPT deformation was successful in redistributing the Cu, Fe and Ag phases. A more detailed analysis of the microstructural evolution of these materials throughout the fabrication process is given in [15]. The chemical composition measured by EDX was documented to be 48.5 at.% Cu, 25.2 at.% Fe and 26.3 at.% Ag and found to be

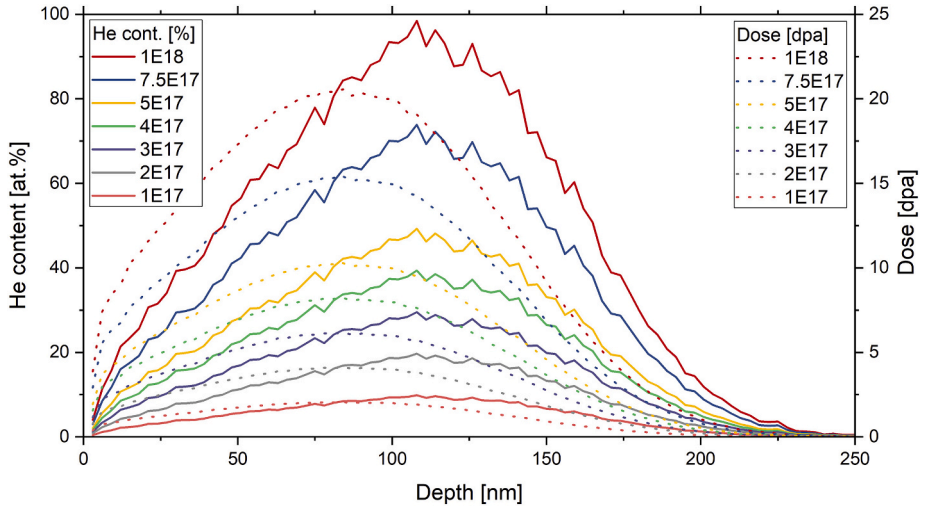

Fig. 1. Helium content (in atomic percent) and radiation dose as a function of implantation depth after irradiation with various fluences of helium.

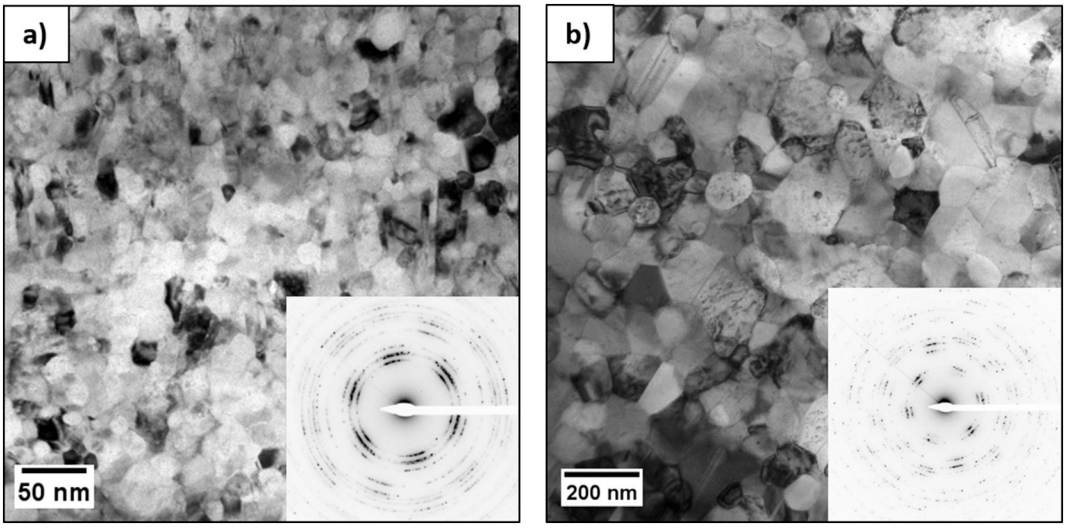

Fig. 2. Bright field TEM images of the microstructure for a) NC and b) UFG Cu-Fe-Ag investigated in this work. Insets represent the respective SAD patterns.

homogeneous over the whole sample volume (the deviation did not exceed ±0.3%).

3.2. Swelling measurements

AFM measurements were conducted to quantify the amount of swelling for each irradiation fluence on both materials. Representative visualizations of the topologies of irradiated areas in NC and UFG material are depicted in Fig. 3a and b, respectively. The helium-implanted squares are clearly visible, as bubble and defect formation lead to swelling and blistering in these areas. Fig. 3c and d represent line scans across the implanted areas for NC and UFG material, respectively. The data for the fluence of 1×10^{17} ions/cm^2 were not included, as they showed no distinction from the unimplanted regions, which was also found in [21] for pure Cu. This indicates that for this dose and below, there is no swelling or the swelling lies within the surface roughness of the sample, which was measured to be about 7 nm for both materials. For better comparison, the average height difference between irradiated and unirradiated areas ("swelling height") as a function of helium fluence is compiled in Fig. 4. While the NC material shows a rather linear swelling behavior with increasing helium dose, the UFG material experiences initially an exponential trend that transitions to a linear behavior for fluences of 5×10^{17} ions/cm^2 and higher.

3.3. Mechanical properties

Nanoindentation experiments were conducted to gather information about elastic and plastic properties of the helium-implanted material. To eliminate possible influences from compressive residual stresses that could have developed during polishing, data from mechanical polishing and ion polishing was compared on the softer UFG material, with a difference in hardness less than 2%, thereby alleviating any concerns on surface preparation artifacts. The analysis of the CSM indentation data is exemplarily demonstrated in Fig. 5 for a specific combination of UFG material and helium fluence. Due to surface effects from the increased surface roughness after implantation, the first 50 nm of indentation were not analyzed. As apparent in Fig. 5, after an indentation depth of 200 nm the values of unirradiated and irradiated indentation curves approach each other. This indicates that at this point the influence of unirradiated material beneath the helium-implanted layer becomes significant and cannot be neglected anymore. Therefore, the analysis of average hardness and modulus was performed for indentation depths between 50 and 200 nm. The results of this analysis are apparent in Figs. 6 and 7. The NC material shows no hardening, but already softening after implantation

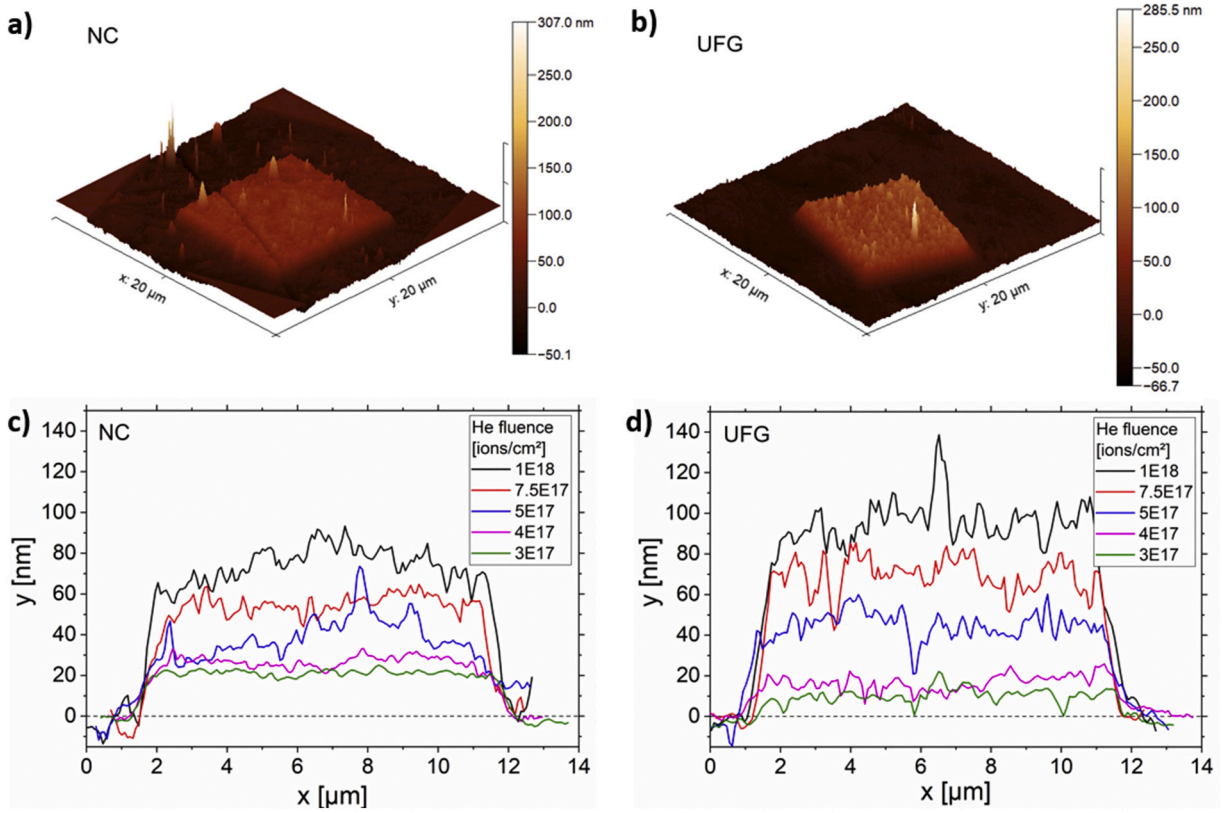

Fig. 3. AFM measurements showing 3-dimensional surface topology reconstructions of the helium-implanted areas in a) NC and b) UFG Cu-Fe-Ag (Fluence = 1E18 ions/cm^2) and AFM line scans of areas implanted with various fluences of helium in c) NC and d) UFG material, respectively.

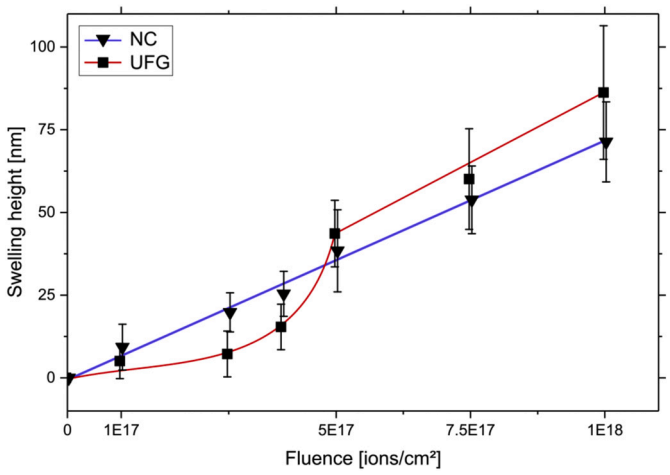

Fig. 4. Average swelling height determined from AFM measurements as a function of helium fluence for NC and UFG material.

with low fluences of helium. Both, hardness and modulus, decrease continuously with increasing amount of implanted helium. For the UFG material, however, the implantations with helium fluences of 1–4 × 10^{17} ions/cm^2 lead to a slight hardening with respect to the unirradiated material. Beyond this point, the higher the implanted helium fluence, the more the hardness decreases, with the hardness for fluences of 5 × 10^{17} to 1 × 10^{18} ions/cm^2 being lower than the unirradiated material. As previously observed for the NC material, the modulus decreases continuously with increasing dose, as expected, since the material gradually turns into a foam-like material [58].

Considering the limited penetration depth of the He implantation (Fig. 1) and the plastic zone probed by nanoindentation being about 3 to 10 times larger than the indent itself [52,53,59], the mechanical properties measured during nanoindentation actually represent the convoluted properties of a layered composite consisting of an irradiated layer on top and unaltered unirradiated material underneath (Fig. 8a). Probing only the properties of the implanted layer by decreasing the indentation depth is extremely challenging due to the aforementioned surface effects, the non-negligible tip defect, and the avoidance of undesired indentation size effects [60]. Therefore, a simple volume fraction model based on models proposed by Hosemann et al. [56] and Kareer et al. [57] was applied in this work to extract properties of only the helium-implanted material layer. It is assumed that the measured composite hardness H_c at a certain indentation depth results from the individual layer hardness H_i times the probed volume fraction of the layer v_i, divided by the whole probed volume:

$$H_c = \frac{\sum H_i \cdot v_i}{\sum v_i} \quad (1)$$

Determining the size of the plastic zone generated by nanoindentation is not a straightforward task, as the mechanisms behind the plastic deformation underneath an indent are a highly discussed topic [52–55]. Basically, Johnson's model [52] correlates the growth of the plastic zone to the expansion of a spherical cavity in an elastic-plastic material and allows an easy approximation of the plastic zone radius c:

$$\left(\frac{c}{a_c}\right)^3 = \frac{1}{3 \cdot tan\theta} \cdot \frac{E}{\sigma_y} \quad (2)$$

Here a_c is the contact radius, θ is the semi-apical angle of the indenter tip (65.27° for a Berkovich tip), E is the elastic modulus and σ_y is the yield strength of the material. The yield strength can be estimated to be 1/2.8 times the hardness for most metals in fully plastic condition. The relation between contact radius and contact area A_c, which is obtained

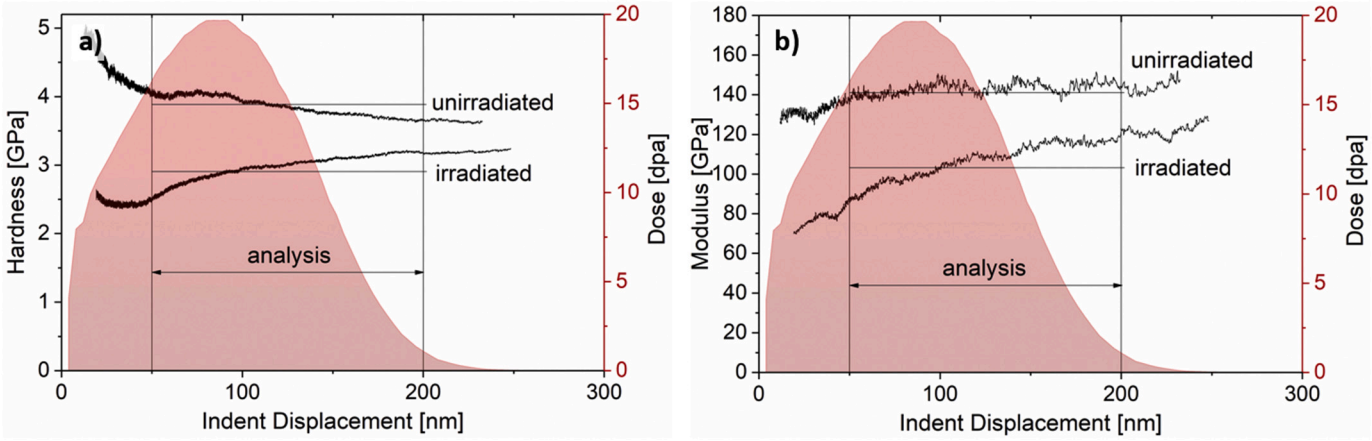

Fig. 5. Analysis of CSM indentation data of UFG sample implanted with 7.5E17 ions/cm^2 for a) hardness and b) Young's modulus. The implanted He dose in dpa is represented by the red-shaded area. (For interpretation of the references to colour in this figure legend, the reader is referred to the web version of this article.)

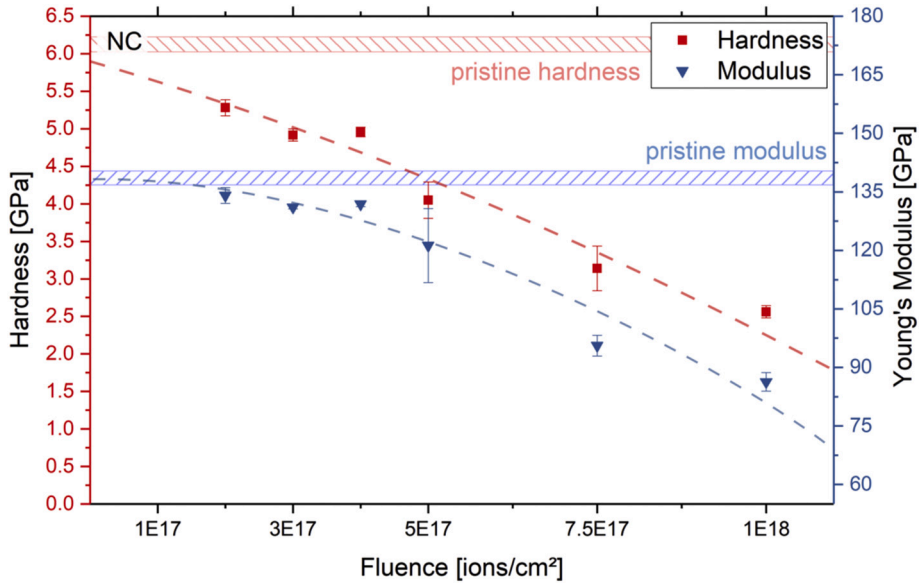

Fig. 6. Hardness and Young's Modulus of NC material implanted with various fluences of helium. The shaded area represents the values for pristine material.

using the Oliver-Pharr method [48], can be approximated for depths exceeding the tip defect via:

$$a_c^2 \cdot \pi = A_c \tag{3}$$

Using the equations above, the plastic zone radius for an indentation depth of 200 nm was calculated to be 890 nm in the UFG material and 800 nm in the NC material, respectively. This of course is reasonable since the NC material is significantly harder than the UFG material.

Assuming a hemispheric plastic zone and an irradiated layer with a thickness of 200 nm plus the swelling height (h_s; compare Fig. 8b), the respective volume fractions can be calculated. Rewriting Eq. (1) and using the unirradiated hardness values gained from the control indents, the hardness of the irradiated layer is calculated by:

$$H_{irr} = \frac{H_c \cdot V_{total} - H_{unirr} \cdot V_{unirr}}{V_{irr}} \tag{4}$$

where H_c was taken from an indentation depth of 200 nm.

The extracted hardness values of the helium-affected zone (if there were no underlying unirradiated material) as well as the relative changes in hardness with respect to the unirradiated materials are depicted in Fig. 9a and b, respectively.

3.4. Post-implantation TEM

To investigate the helium bubble structure after implantation, lift-outs were taken from the NC material implanted with fluences of 3 × 10^{17} and 1 × 10^{18} ions/cm^2. Fig. 10a shows a STEM image of the cross-section of the helium-implanted layer in the NC material implanted with 3 × 10^{17} ions/cm^2. Bubbles are clearly visible with different sizes. Examples of medium-sized bubbles with a diameter of 10–20 nm are marked by arrows 1–3, while smaller bubbles with a diameter below 10 nm are indicated by arrows 4–6. Fig. 10b and c) show underfocused bright field TEM images of the largest bubbles observed in the material implanted with 3 × 10^{17} and 1 × 10^{18} ions/cm^2, respectively.

4. Discussion

In the remainder, we will first focus on the experimentally observed microstructure-dependent swelling behavior, before turning to the mechanistic description of the resultant modifications in mechanical properties.

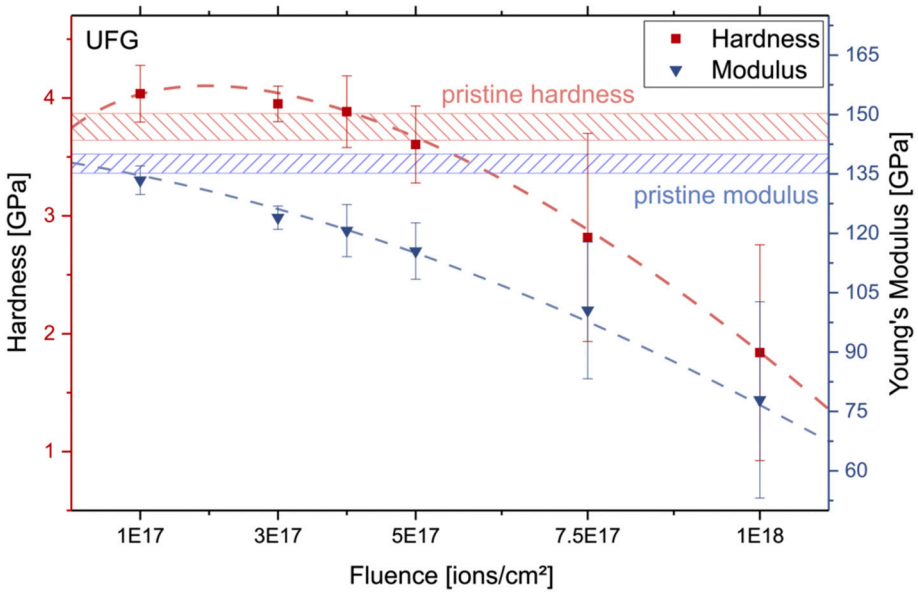

Fig. 7. Hardness and Young's Modulus of UFG material implanted with various fluences of helium. The shaded area represents the values for pristine material.

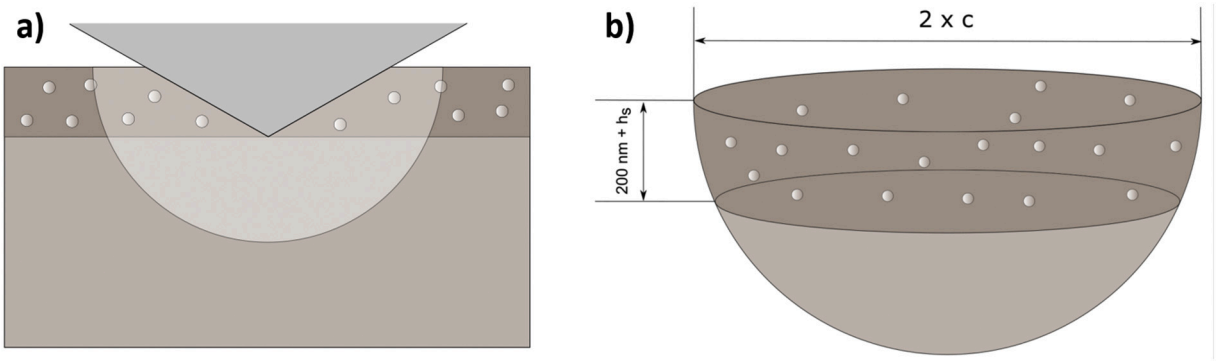

Fig. 8. a) Sketch of the indentation and plastic zone probed in helium implanted material. b) Schematic of the plastic zone probed during indentation and the differently affected material volumes within.

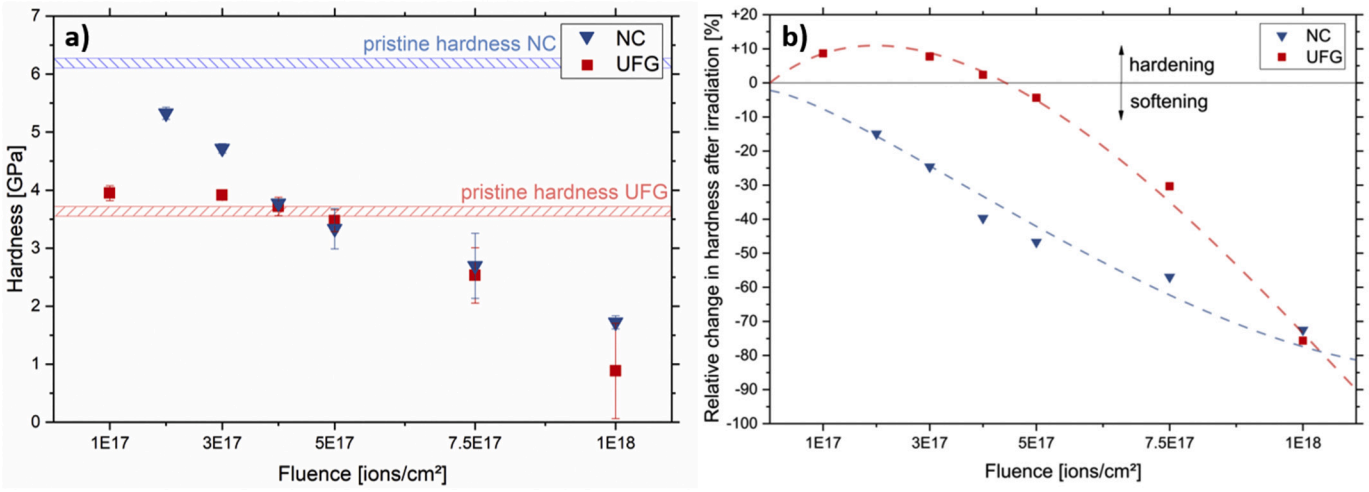

Fig. 9. a) Extracted hardness of the helium-implanted layer by applying the volume-fraction model. b) Relative hardness changes of the helium implanted materials compared to the pristine conditions.

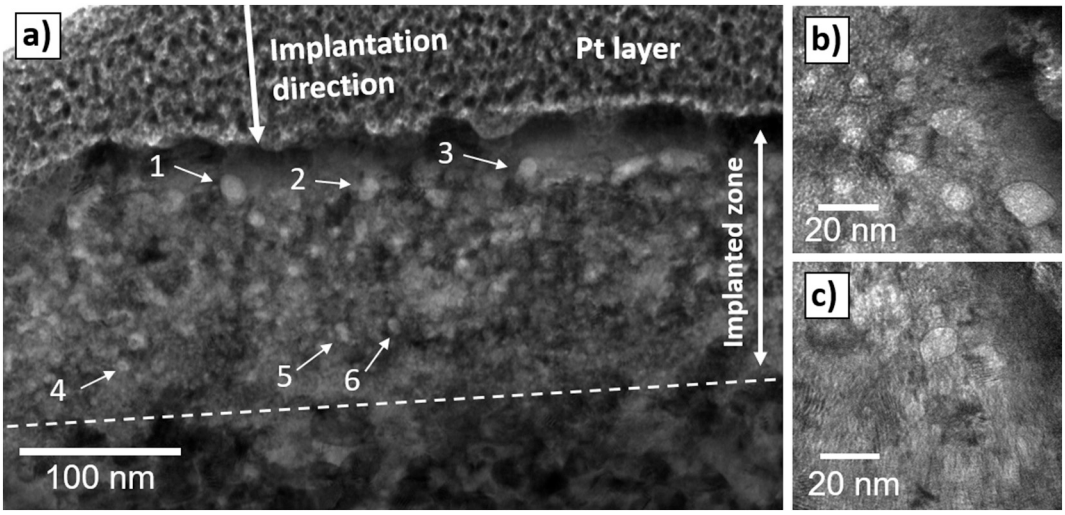

Fig. 10. a) STEM image of helium bubbles formed in NC Cu-Fe-Ag after implantation with 3×10^{17} ions/cm^2. Arrows mark the formation of medium sized (1–3) and small (4–6) bubbles. b, c) Bright field TEM images of the largest bubbles observed in NC material implanted with 3×10^{17} and 1×10^{18} ions/cm^2, respectively.

4.1. Swelling

Intuitively one would expect that the NC material swells less than the UFG material since the interfaces created by the GB are able to absorb more defects making the NC material more radiation tolerant [13–15]. This is the basis for multilayer materials as studied in [8,9,12]. While this of course is generally true, one does have to distinguish between void swelling and helium or gas swelling as well as the nature of the interfaces. Our research presented here find that this general assumption is oversimplified and in some circumstances a less predictable behavior may occur.

Swelling of helium-irradiated materials is directly correlated to size and density of helium bubbles and He-vacancy clusters. The two materials investigated here experienced a rather different swelling behavior with increasing helium fluence (Fig. 4). For the sake of simplicity, the mechanisms for the low fluence (1×10^{17}–5×10^{17} ions/cm^2) and high fluence (5×10^{17}–1×10^{18} ions/cm^2) regimes will be discussed separately.

For low fluences, the swelling in the UFG material depicts an initial incubation period followed by exponential growth up to 5×10^{17} ions/cm^2. Previous work performed may not have captured this difference since in Y. Yang's Cu implantation [21] only 1×10^{17} ions/cm^2 and 5×10^{17} ions/cm^2 was conducted with no steps in between. Interestingly the swelling values in pure Cu are not too dissimilar than the swelling values shown here. The different initial swelling rates at the lower fluence regime may originate from the fact that at low fluences the initial helium bubble nucleation plays a significant role. In order to form a bubble, sufficient amount of helium and vacancies must form a gas cavity large enough to be stable and grow. This initial nucleation process is governed by the distance the defects can migrate and if heterogeneous or homogeneous nucleation occurs.

The NC material has a significant amount of interfaces that act as trapping sites for He but also foster interfacial diffusion which is significantly faster than bulk diffusion. Therefore, it is not hard to imagine that initially helium is trapped at these interfaces and the interfaces (having high energy) easily can foster the nucleation of helium bubbles since it reduces the energy needed to form a fresh surface. Thus, we propose that at these very high dose rates and doses (1×10^{17} corresponds to ~8% helium) as used here, helium bubbles will nucleate rather rapidly on pre-existing defects (grain boundaries). This has also been observed in previous works [25,27,30]. The distance the defects can travel are limited while grain boundaries are fostering heterogeneous nucleation in the NC material. This would lead to a direct relationship between helium content and swelling, reducing the initial nucleation phase. It is interesting to note, however, that this relationship is nearly linear while one would assume a more parabolic relationship. However, this may originate from the fact that the amount of helium implanted here is very large.

If the above argument on nucleation and growth is true, one would also expect a delayed nucleation and growth in the UFG material since less nucleation sites exist. Here the helium-ions will remain isolated within the grain interior or form small He-vacancy clusters. With increasing fluence, more insoluble helium is implanted in the material, thereby increasing the chances for helium atoms to form bubbles. The more these bubbles consecutively grow, the easier they attract additional helium-ions, explaining the exponential growth. The above discussed mechanisms for helium accommodation and bubble formation at low helium fluence are illustrated in Fig. 11. Due to demonstrative reasons, the grain size of the UFG material in this sketch is only twice as big as in NC material (instead of the actual five times difference).

At high fluences both materials demonstrate a similar linear swelling trend, with the absolute values of the UFG material amounting slightly above the NC material. At these fluences, there is enough helium implanted to effortlessly form bubbles homogeneously in both materials. The difference in swelling of the two microstructures is once again related to the interface density: the growth of bubbles within the grain interior in the NC material is retarded by the smaller grain size and closer interface spacing, since the interfaces as efficient defect sinks prohibit growth of the bubbles. This has also been observed in previous works on nanostructured Cu-based composite alloys [7,32–35]. Hattar et al. [33] attribute the prohibited growth of bubbles to the immiscibility of the individual components, hindering vacancies from diffusing across the interfaces and contributing to the growth of He-vacancy clusters. Comparing the surface topologies scanned by AFM (Fig. 3a and b) confirms this assumption. The UFG material shows a few large blisters with an approximate diameter of 300 nm, but the majority of blisters have dimensions below 100 nm. In the NC material even fewer larger blisters form, and the remaining ones are considerably smaller than what is observed for the UFG material. This characteristic in combination with the fact that there is a larger amount of nucleation sites in the NC material causes the bubbles to be smaller but of higher number than in the UFG material. Furthermore, it is established that large helium bubbles contain a higher amount of vacancies, which results in underpressurization and more swelling as compared to small bubbles [17,19,21,24]. In the NC material it is presumed that vacancies generated by the displacement damage of the ions will primarily diffuse to and

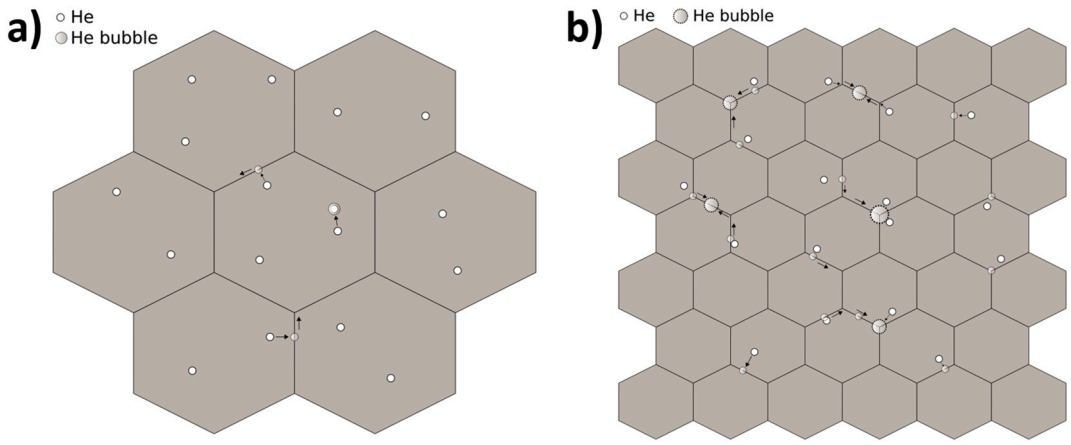

Fig. 11. Suggested mechanisms for helium accommodation and bubble formation for the low fluence regime in a) UFG and b) NC material. Helium remains isolated or forms small helium bubbles in the grain interior in the UFG material, while the large amount and close proximity of interfaces in the NC material facilitates diffusion of helium and easier nucleation of medium-sized bubbles at grain boundaries and triple junctions.

annihilate at grain boundaries, rather than contributing to formation and growth of helium-vacancy clusters, while for the UFG material the considerably lower density of grain boundaries results in excess vacancies and therefore easier growth of bubbles and He-vacancy clusters. Thus, the slightly lower swelling in NC material at high He fluences is explained by a higher density of interfaces as illustrated in Fig. 12.

It is worth noting that the change from an exponential to a linear behavior in swelling of the UFG sample (Fig. 4) might indicate a transition from free growth of bubbles in the grain interior to a more restricted growth and preferred nucleation of new bubbles since the existing ones are approaching the grain size. A detailed examination of this behavior, however, is beyond the scope of this work.

4.2. Mechanical properties

The results from nanoindentation tests (Figs. 6 and 7) are in good agreement with the swelling model suggested above. While for the UFG material the hardness is increased at low helium fluences and decreased at high fluences, the NC material shows a continuously decreasing hardness for all helium fluences tested within this work. The isolated He ions and small bubbles present in the UFG material at low doses act as obstacles to dislocation movement, which gives rise to the observed hardening [20]. The higher the helium content, and therefore bubble size and density, the more the material behaves in analogy to a foam and consequently the hardness decreases. In the NC material, the easier bubble nucleation results in a higher bubble population for low doses. This leads to a foam-like characteristic and a slight softening effect already for low amounts of helium, which turns more pronounced the higher the helium fluence becomes. The continuous decrease in measured Young's modulus is as expected, since the bubble size and density increase with increasing amount of helium.

The hardness values extracted by employing the volume fraction model (Fig. 9a) and the relative change in hardness (Fig. 9b) are in line with general behavior discussed above, supporting the suggested mechanisms for bubble nucleation and growth. It is also noticeable in this data that for the highest fluences investigated in this study, the degradation of mechanical properties in UFG material follows a much steeper trend than in NC material, indicating a complete collapse of the structure for high fluences of helium. The stress state and plastic zone beneath an indent, as well as the distribution of helium within the material, are of course much more complex than assumed by the volume fraction model in this work, yet the gained hardness values seem plausible and suggest eligibility of this model for straight forward approximation of mechanical properties of differently affected material layers.

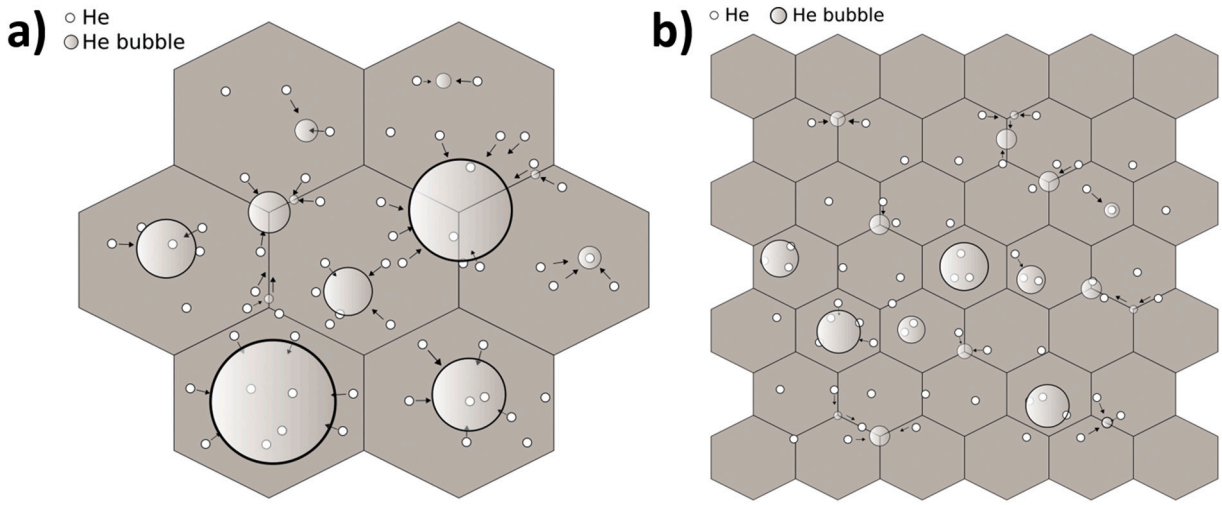

Fig. 12. Suggested mechanisms for helium bubble nucleation and growth for the high fluence regime in a) UFG and b) NC material. Helium bubble growth is more restricted and stable in the NC material, which results in smaller bubble size and therefore less swelling.

4.3. Post-implantation TEM

In order to verify the mechanisms suggested by swelling and indentation measurements, lift-outs of implanted areas in NC material were performed and investigated in the TEM. The particular fluences of 3×10^{17} and 1×10^{18} ions/cm^2 on the NC sample were chosen for the TEM investigation after evaluating the AFM and nanoindentation results and were deemed the most promising to confirm the derived mechanisms of bubble nucleation and growth. From the overview STEM image of fluence 3×10^{17} ions/cm^2 in Fig. 10a it is seen that already medium-sized bubbles (arrows 1–3) with diameters ranging between 10 and 20 nm are present, indicating a facilitated bubble formation in the NC material for this low fluence regime, as suggested above. It is also apparent that deeper below the surface, where the radiation dose and helium content is supposed to be significantly lower, there is also a respectable amount of smaller bubbles, supporting the argument of easier bubble nucleation in NC material. Due to the small grain size of the material, it is unavoidable to look at multiple grains and, consequently, grain boundaries throughout the thickness direction of the TEM lift-out. Therefore, it cannot be confirmed whether the bubbles nucleate primarily on grain boundaries and triple junctions, however, it is a logical explanation to the observed swelling and mechanical property response of this material. The biggest bubbles found in the lift-out samples of both investigated fluences are depicted in Fig. 10b (3×10^{17} ions/cm^2) and c (1×10^{18} ions/cm^2). It is immediately evident that the bubble sizes are comparable and below or in the range of the average grain size (18.8 nm), indicating that once the bubbles reach this size, it is more favorable to nucleate new bubbles upon further helium implantation instead of making them grow further, which is in agreement to the hypothesized model drawn from swelling and hardness measurements described above. It is noted that these bubble sizes are large compared to bubbles observed in previous works on nanostructured Cu alloys after room temperature irradiation [32,33,35]. The high fluences of helium investigated in this work will lead to much more helium as well as radiation-induced vacancies in the material. This is considered to promote easier bubble growth compared to low fluence irradiation and results in the bubble sizes seen in Fig. 10.

5. Conclusion

In this work, NC and UFG variants of a Cu-Fe-Ag metallic composite material containing different densities of phase boundaries were implanted with various amounts of helium. Using AFM and nanoindentation, the dependency of swelling and changes in mechanical properties on grain size and helium fluence were investigated. The results were utilized to derive possible mechanisms for nucleation and growth of helium bubbles within these materials, and post-implantation TEM was applied to verify these models. It was observed that for low fluences of helium, the closer spacing of interfaces in the NC material promotes diffusion of helium and consequently bubble nucleation and growth. For higher helium fluences, the small grain size of the NC material restricts bubble growth. The UFG material shows an incubation period for bubble nucleation for low helium fluences, but pronounced bubble growth for higher fluences. As the grain size in the UFG material of 100 nm is still relatively small compared to conventional materials, one can expect that this enhanced bubble growth is even more pronounced in coarse-grained metals, as there are significantly fewer grain and phase boundaries to restrict growth, but more vacancies available in the grain interior to contribute to He-vacancy cluster growth. Therefore, it is concluded that smaller grain sizes promote bubble nucleation, but also cause more stable bubble growth, since they are being nucleated and pinned at grain boundaries. While for low fluences of helium this results in a better performance of UFG materials regarding swelling, one should not neglect the fact that the small He-vacancy clusters created will act as dislocation obstacles and lead to embrittlement of the material. As interfaces are diverse in terms of structure, sink efficiency and helium storage capability, different bubble size and density are expected for a given fluence and grain size in specific materials. However, the general mechanisms for bubble nucleation and growth in metallic materials is expected to still follow the model proposed herein, with minor changes in thresholds and correlations regarding bubble size, density, helium fluence and grain size. Previous works suggest that the immiscibility of the individual components plays a key role in constricting bubble growth at the interfaces, which would result in worse performance of single-phase nanocrystalline materials compared to the present nanocomposites. Future investigations on nanostructured single-phase materials should confirm this behavior. In conclusion, the already demonstrated radiation tolerance of the NC material, together with the relatively good performance after exposure to high fluences of helium demonstrated in this work, make a strong case for deployment of nanocrystalline (composite) materials in a combined neutron- and helium-irradiative environment in next generation nuclear facilities.

Data availability

The datasets generated during the current study are available from the corresponding author on reasonable request.

Declaration of Competing Interest

The authors declare that they have no known competing financial interests or personal relationships that could have appeared to influence the work reported in this paper.

Acknowledgements

The financial support by the Austrian Marshall Plan Foundation and the Montanuniversität Leoben, Austria is gratefully acknowledged. The authors also acknowledge funding by the European Research Council, European Union under Grant numbers: 771146 (MW, II, DK) and 757333 (AB). Instrument access was provided in part through the Biomolecular Nanotechnology Center (BNC) at UC Berkeley. Additional support was provided by NSF-DMR Program, USA number 1807822. The authors thank Dr. Verena Maier-Kiener for validation measurements using her G200 nanoindenter.

References

[1] J. Parsons, J. Buongiorno, M. Corradini, D. Petti, A fresh look at nuclear energy, Science 363 (2019) 105, https://doi.org/10.1126/science.aaw5304.
[2] B.W. Brook, A. Alonso, D.A. Meneley, J. Misak, T. Blees, J.B. Van Erp, Why nuclear energy is sustainable and has to be part of the energy mix, Sustain. Mater. Technol. 1–2 (2014) 8–16, https://doi.org/10.1016/j.susmat.2014.11.001.
[3] S.J. Zinkle, Fusion materials science: overview of challenges and recent progress, Phys. Plasmas. 12 (2005), 058101, https://doi.org/10.1063/1.1880013.
[4] S.J. Zinkle, Advanced materials for fusion technology, Fusion Eng. Des. 74 (2005) 31–40, https://doi.org/10.1016/j.fusengdes.2005.08.008.
[5] P. Yvon, F. Carré, Structural materials challenges for advanced reactor systems, J. Nucl. Mater. 385 (2009) 217–222, https://doi.org/10.1016/j.jnucmat.2008.11.026.
[6] S.J. Zinkle, G.S. Was, Materials challenges in nuclear energy, Acta Mater. 61 (2013) 735–758, https://doi.org/10.1016/j.actamat.2012.11.004.
[7] X. Zhang, K. Hattar, Y. Chen, L. Shao, J. Li, C. Sun, K. Yu, N. Li, M.L. Taheri, H. Wang, J. Wang, M. Nastasi, Radiation damage in nanostructured materials, Prog. Mater. Sci. 96 (2018) 217–321, https://doi.org/10.1016/j.pmatsci.2018.03.002.
[8] A. Misra, M.J. Demkowicz, X. Zhang, R.G. Hoagland, The radiation damage tolerance of ultra-high strength Nanolayered composites, JOM. 59 (2007) 3–6, https://doi.org/10.1007/s11837-007-0120-6.
[9] M.J. Demkowicz, R.G. Hoagland, J.P. Hirth, Interface structure and radiation damage resistance in Cu-Nb multilayer nanocomposites, Phys. Rev. Lett. 100 (2008) 2–5, https://doi.org/10.1103/PhysRevLett.100.136102.
[10] S. Wurster, R. Pippan, Nanostructured metals under irradiation, Scr. Mater. 60 (2009) 1083–1087, https://doi.org/10.1016/j.scriptamat.2009.01.011.
[11] E.M. Bringa, J.D. Monk, A. Caro, A. Misra, L.A. Zepeda-Ruiz, M. Duchaineau, F. Abraham, M. Nastasi, S.T. Picraux, Y. Wang, D. Farkas, Are nanoporous materials radiation resistant? Nano Lett. 12 (2012) 3351–3355, https://doi.org/10.1021/nl201383u.

[12] W. Han, M.J. Demkowicz, N.A. Mara, E.G. Fu, S. Sinha, A.D. Rollett, Y. Wang, J. S. Carpenter, I.J. Beyerlein, A. Misra, Design of radiation tolerant materials via interface engineering, Adv. Mater. 25 (2013) 6975–6979, https://doi.org/10.1002/adma.201303400.
[13] I.J. Beyerlein, A. Caro, M.J. Demkowicz, N.A. Mara, A. Misra, B.P. Uberuaga, Radiation damage tolerant nanomaterials, Mater. Today 16 (2013) 443–449, https://doi.org/10.1016/j.mattod.2013.10.019.
[14] I.J. Beyerlein, M.J. Demkowicz, A. Misra, B.P. Uberuaga, Defect-interface interactions, Prog. Mater. Sci. 74 (2015) 125–210, https://doi.org/10.1016/j.pmatsci.2015.02.001.
[15] M. Wurmshuber, D. Frazer, A. Bachmaier, Y. Wang, P. Hosemann, D. Kiener, Impact of interfaces on the radiation response and underlying defect recovery mechanisms in nanostructured Cu-Fe-Ag, Mater. Des. 160 (2018) 1148–1157, https://doi.org/10.1016/j.matdes.2018.11.007.
[16] C. Howard, V. Bhakhri, C. Dixon, H. Rajakumar, C. Mayhew, C.D. Judge, Coupling multi-scale mechanical testing techniques reveals the existence of a trans-granular channel fracture deformation mechanism in high dose Inconel X-750, J. Nucl. Mater. 517 (2019) 17–34, https://doi.org/10.1016/j.jnucmat.2019.01.051.
[17] D.R. Olander, Fundamental Aspects of Nuclear Reactor Fuel Elements, Technical Information Center, Office of Public Affairs, Energy Research and Development Administration, Springfield, USA, 1977, https://doi.org/10.1016/0022-3115(77)90226-4.
[18] C. Cawthorne, W.J. Fulton, Voids in irradiated stainless steel, Nature. 216 (1967) 575–576, https://doi.org/10.1038/216575a0.
[19] H. Trinkaus, B.N. Singh, Helium accumulation in metals during irradiation – where do we stand? J. Nucl. Mater. 323 (2003) 229–242, https://doi.org/10.1016/j.jnucmat.2003.09.001.
[20] K. Yu, Y. Liu, C. Sun, H. Wang, L. Shao, E.G. Fu, X. Zhang, Radiation damage in helium ion irradiated nanocrystalline Fe, J. Nucl. Mater. 425 (2012) 140–146, https://doi.org/10.1016/j.jnucmat.2011.10.052.
[21] Y. Yang, D. Frazer, M. Balooch, P. Hosemann, Irradiation damage investigation of helium implanted polycrystalline copper, J. Nucl. Mater. 512 (2018) 137–143, https://doi.org/10.1016/j.jnucmat.2018.09.022.
[22] W.S. Cunningham, J.M. Gentile, O. El-atwani, C.N. Taylor, M. Efe, S.A. Maloy, J. R. Trelewicz, Softening due to grain boundary cavity formation and its competition with hardening in helium implanted Nanocrystalline tungsten, Sci. Rep. 8 (2018) 1–10, https://doi.org/10.1038/s41598-018-20990-1.
[23] O. El-Atwani, W.S. Cunningham, D. Perez, E. Martinez, J.R. Trelewicz, M. Li, S. A. Maloy, Temperature threshold for preferential bubble formation on grain boundaries in tungsten under in-situ helium irradiation, Scr. Mater. 180 (2020) 6–10, https://doi.org/10.1016/j.scriptamat.2020.01.013.
[24] W. Han, E.G. Fu, M.J. Demkowicz, Y. Wang, A. Misra, Irradiation damage of single crystal, coarse-grained, and nanograined copper under helium bombardment at 450°C, J. Mater. Res. 28 (2013) 2763–2770, https://doi.org/10.1557/jmr.2013.283.
[25] O. El-Atwani, J.A. Hinks, G. Greaves, S. Gonderman, T. Qiu, M. Efe, J.P. Allain, In-situ TEM observation of the response of ultrafine- and nanocrystalline-grained tungsten to extreme irradiation environments, Sci. Rep. 4 (2014) 4–10, https://doi.org/10.1038/srep04716.
[26] O. El-Atwani, S. Gonderman, M. Efe, G. De Temmerman, T. Morgan, K. Bystrov, D. Klenosky, T. Qiu, J.P. Allain, Ultrafine tungsten as a plasma-facing component in fusion devices: effect of high flux, high fluence low energy helium irradiation, Nucl. Fusion. 54 (2014), https://doi.org/10.1088/0029-5515/54/8/083013.
[27] O. El-Atwani, K. Hattar, J.A. Hinks, G. Greaves, S.S. Harilal, A. Hassanein, Helium bubble formation in ultrafine and nanocrystalline tungsten under different extreme conditions, J. Nucl. Mater. 458 (2015) 216–223, https://doi.org/10.1016/j.jnucmat.2014.12.095.
[28] O. El-Atwani, J.E. Nathaniel, A.C. Leff, K. Hattar, M.L. Taheri, Direct observation of sink-dependent defect evolution in nanocrystalline iron under irradiation, Sci. Rep. 7 (2017) 1–12, https://doi.org/10.1038/s41598-017-01744-.
[29] O. El-Atwani, J.A. Hinks, G. Greaves, J.P. Allain, S.A. Maloy, Grain size threshold for enhanced irradiation resistance in nanocrystalline and ultrafine tungsten, Mater. Res. Lett. 5 (2017) 343–349, https://doi.org/10.1080/21663831.2017.1292326.
[30] O. El-Atwani, J.E. Nathaniel, A.C. Leff, B. Muntifering, J.K. Baldwin, K. Hattar, M. L. Taheri, The role of grain size in He bubble formation: implications for swelling resistance, J. Nucl. Mater. 484 (2017) 236–244, https://doi.org/10.1016/j.jnucmat.2016.12.003.
[31] Z. Chen, L.L. Niu, Z. Wang, L. Tian, L. Kecskes, K. Zhu, Q. Wei, A comparative study on the in situ helium irradiation behavior of tungsten: Coarse grain vs. nanocrystalline grain, Acta Mater. 147 (2018) 100–112, https://doi.org/10.1016/j.actamat.2018.01.015.
[32] T. Höchbauer, A. Misra, K. Hattar, R.G. Hoagland, Influence of interfaces on the storage of ion-implanted he in multilayered metallic composites influence of interfaces on the storage of ion-implanted he in multilayered, J. Appl. Phys. 98 (2005) 123516, https://doi.org/10.1063/1.2149168.
[33] K. Hattar, M.J. Demkowicz, A. Misra, I.M. Robertson, R.G. Hoagland, Arrest of He bubble growth in Cu – Nb multilayer nanocomposites, Scr. Mater. 58 (2008) 541–544, https://doi.org/10.1016/j.scriptamat.2007.11.007.
[34] N. Li, J.J. Carter, A. Misra, L. Shao, H. Wang, X. Zhang, N. Li, J.J. Carter, A. Misra, L. Shao, H. Wang, X.Z. The, The Influence of Interfaces on the Formation of Bubbles in He-Ion-Irradiated Cu/Mo Nanolayers, 2011, p. 0839, https://doi.org/10.1080/09500839.2010.522210.
[35] W.Z. Han, N.A. Mara, Y.Q. Wang, A. Misra, M.J. Demkowicz, He implantation of bulk Cu – Nb nanocomposites fabricated by accumulated roll bonding, J. Nucl. Mater. 452 (2014) 57–60, https://doi.org/10.1016/j.jnucmat.2014.04.034.
[36] E.G. Fu, A. Misra, H. Wang, L. Shao, X. Zhang, Interface enabled defects reduction in helium ion irradiated Cu/V Nanolayers, J. Nucl. Mater. 407 (2010) 178–188, https://doi.org/10.1016/j.jnucmat.2010.10.011.
[37] J.S. Song, S.I. Hong, H.S. Kim, Heavily drawn Cu-Fe-Ag and Cu-Fe-Cr microcomposites, J. Mater. Process. Technol. 113 (2001) 610–616, https://doi.org/10.1016/S0924-0136(01)00665-3.
[38] H. Gao, J. Wang, D. Shu, B. Sun, Effect of Ag on the microstructure and properties of Cu-Fe in situ composites, Scr. Mater. 53 (2005) 1105–1109, https://doi.org/10.1016/j.scriptamat.2005.07.028.
[39] J.S. Song, S.I. Hong, Y.G. Park, Deformation processing and strength/conductivity properties of Cu-Fe-Ag microcomposites, J. Alloys Compd. 388 (2005) 69–74, https://doi.org/10.1016/j.jallcom.2004.07.013.
[40] B. Sun, H. Gao, J. Wang, D. Shu, Strength of deformation processed Cu-Fe-Ag in situ composites, Mater. Lett. 61 (2007) 1002–1006, https://doi.org/10.1016/j.matlet.2006.06.030.
[41] J. Wang, P. Xiong, G. Xiao, Investigation of giant magnetoresistance in concentrated and nanstructured alloys, Phys. Rev. B 47 (1993) 8341–8344, https://doi.org/10.1103/physrevb.47.8341.
[42] N.S. Cohen, E. Ahlswede, J.D. Wicks, Q.A. Pankhurst, Investigation of the ternary phase diagram of mechanically alloyed FeCuAg, J. Phys. Condens. Matter 9 (1997) 3259–3276, https://doi.org/10.1088/0953-8984/9/15/016.
[43] Q.A. Pankhurst, N.S. Cohen, M. Odlyha, Thermal analysis of metastable Fe-Cu-Ag prepared by mechanical alloying, J. Phys. Condens. Matter 10 (1998) 1665–1676, https://doi.org/10.1088/0953-8984/10/7/014.
[44] R. Pippan, S. Scheriau, A. Hohenwarter, M. Hafok, Advantages and limitations of HPT: a review, Mater. Sci. Forum 584–586 (2008) 16–21, https://doi.org/10.4028/www.scientific.net/MSF.584-586.16.
[45] J.F. Ziegler, J.P. Biersack, SRIM - The Stopping and Range of Ions in Solids, 1985.
[46] Z.J. Wang, F.I. Allen, Z.W. Shan, P. Hosemann, Mechanical behavior of copper containing a gas-bubble superlattice, Acta Mater. 121 (2016) 78–84, https://doi.org/10.1016/j.actamat.2016.08.085.
[47] A.M. Robinson, P.D. Edmondson, C. English, S. Lozano-perez, G. Greaves, J. A. Hinks, S.E. Donnelly, C.R.M. Grovenor, The effect of temperature on bubble lattice formation in copper under in situ he ion irradiation, Scr. Mater. 131 (2017) 108–111, https://doi.org/10.1016/j.scriptamat.2016.12.031.
[48] W.C. Oliver, G.M. Pharr, An improved technique for determining hardness and elastic modulus using load and displacement sensing indentation experiments, J. Mater. Res. 7 (1992) 1564–1583, https://doi.org/10.1557/JMR.1992.1564.
[49] W.C. Oliver, G.M. Pharr, Measurement of hardness and elastic modulus by instrumented indentation: advances in understanding and refinements to methodology, J. Mater. Res. 19 (2004), https://doi.org/10.1557/jmr.2004.19.1.3.
[50] G.M. Pharr, J.H. Strader, W.C. Oliver, Critical issues in making small-depth mechanical property measurements by nanoindentation with continuous stiffness measurement, J. Mater. Res. 24 (2009) 653–666, https://doi.org/10.1557/JMR.2009.0096.
[51] A. Leitner, V. Maier-Kiener, D. Kiener, Dynamic nanoindentation testing: is there an influence on a material's hardness? Mater. Res. Lett. 5 (2017) 486–493, https://doi.org/10.1080/21663831.2017.1331384.
[52] K.L. Johnson, The correlation of indentation experiments, J. Mech. Phys. Solids. 18 (1970) 115–126, https://doi.org/10.1016/0022-5096(70)90029-3.
[53] M. Mata, O. Casals, J. Alcalá, The plastic zone size in indentation experiments: The analogy with the expansion of a spherical cavity, Int. J. Solids Struct. 43 (2006) 5994–6013, https://doi.org/10.1016/j.ijsolstr.2005.07.002.
[54] D. Kiener, A.M. Minor, O. Anderoglu, Y. Wang, S.A. Maloy, P. Hosemann, Application of small-scale testing for investigation of ion-beam-irradiated materials, J. Mater. Res. 27 (2012) 2724–2736, https://doi.org/10.1557/jmr.2012.303.
[55] P. Hosemann, C. Shin, D. Kiener, Small scale mechanical testing of irradiated materials, J. Mater. Res. 30 (2015) 1231–1245, https://doi.org/10.1557/jmr.2015.26.
[56] P. Hosemann, D. Kiener, Y. Wang, S.A. Maloy, Issues to consider using nano indentation on shallow ion beam irradiated materials, J. Nucl. Mater. 425 (2012) 136–139, https://doi.org/10.1016/j.jnucmat.2011.11.070.
[57] A. Kareer, A. Prasitthipayong, D. Krumwiede, D.M. Collins, P. Hosemann, S. G. Roberts, An analytical method to extract irradiation hardening from nanoindentation hardness-depth curves, J. Nucl. Mater. 498 (2018) 274–281, https://doi.org/10.1016/j.jnucmat.2017.10.049.
[58] L.J. Gibson, M.F. Ashby, Cellular Solids - Structure and Properties, 1997.
[59] D. Kiener, R. Pippan, C. Motz, H. Kreuzer, Microstructural evolution of the deformed volume beneath microindents in tungsten and copper, Acta Mater. 54 (2006) 2801–2811, https://doi.org/10.1016/j.actamat.2006.02.024.
[60] W.D. Nix, H. Gao, Indentation size effects in crystalline materials: a law for strain gradient plasticity, J. Mech. Phys. Solids. 46 (1998) 411–425, https://doi.org/10.1016/s0022-5096(97)00086-0.